

IRDC G030.88+00.13: A Tale of Two Massive Clumps

Qizhou Zhang¹, Ke Wang^{1,2}

qzhang@cfa.harvard.edu

ABSTRACT

Massive stars ($M \gtrsim 10 M_{\odot}$) form from collapse of parsec-scale molecular clumps. How molecular clumps fragment to give rise to massive stars in a cluster with a distribution of masses is unclear. We search for cold cores that may lead to future formation of massive stars in a massive ($> 10^3 M_{\odot}$), low luminosity ($4.6 \times 10^2 L_{\odot}$) infrared dark cloud (IRDC) G030.88+00.13. The NH_3 data from VLA and GBT reveal that the extinction feature seen in the infrared consists of two distinctive clumps along the same line of sight: The C1 clump at 97 km s^{-1} coincides with the extinction in the Spitzer 8 and $24 \mu\text{m}$. Therefore, it is responsible for the majority of the IRDC. The C2 clump at 107 km s^{-1} is more compact and has a peak temperature of 45 K. Compact dust cores and H_2O masers revealed in the SMA and VLA observations are mostly associated with C2, and none is within the IRDC in C1. The luminosity indicates that neither the C1 nor C2 clump has yet to form massive protostars. But C1 might be at a precluster forming stage. The simulated observations rule out 0.1pc cold cores with masses above $8 M_{\odot}$ within the IRDC. The core masses in C1 and C2, and those in high-mass protostellar objects suggest an evolutionary trend that the mass of cold cores increases over time. Based on our findings, we propose an empirical picture of massive star formation that protostellar cores and the embedded protostars undergo simultaneous mass growth during the protostellar evolution.

Subject headings: ISM: clouds - ISM: individual (G030+00.13) - ISM: kinematics and dynamics - stars: formation

1. Introduction

It is well known that massive stars form in clusters that contain a distribution of stellar masses (Lada & Lada 2003). How dense molecular clouds contract and fragment to give rise

¹Harvard-Smithsonian Center for Astrophysics, 60 Garden Street, Cambridge MA 02138, USA

²Department of Astronomy, School of Physics, Peking University, Beijing 100871, China

to a cluster of stars has been a subject of intense studies for decades. It is often suggested that the stellar mass at the peak of the Initial Stellar Function (IMF) is related to and perhaps is determined by the characteristic mass in molecular clouds. The value of such mass is dictated by the interplay of gravity, internal pressure due to thermal and turbulent motions, and/or magnetic fields (Larson 2005). A typical proto cluster forming clump¹ with massive young stellar objects contains $10^3 M_\odot$ of dense molecular gas (Molinari et al. 2000; Beuther et al. 2002; Beltrán et al. 2006) within a size scale of about 1 pc. The average density (10^5 cm^{-3}) and temperature (15 K) (Rathborne et al. 2007; Pillai et al. 2006) in these clumps yield a Jeans mass² of approximately $1 M_\odot$. This characteristic mass explains naturally the peak of the IMF in a cluster (Larson 2005).

Massive stars, on the other hand, contain masses at least an order of magnitude larger than the global thermal Jean mass in a molecular clump. This presents a theoretical puzzle, since cores and stars significantly larger than the global Jeans mass are unstable against fragmentations to less massive objects. While the origin of low mass stars could be linked to the Jeans mass, how massive stars form in a cluster has been a matter of debate. Do massive stars form in cores of Jeans mass similar to their low mass counterpart, or form in cores far more massive than the thermal Jeans mass? Observations of high-mass protostellar objects often find hot molecular cores with masses of $10 - 10^2 M_\odot$ (Garay & Lizano 1999), consistent with Jeans mass at elevated gas temperatures of over 100 K. However, the typical Jeans mass in a molecular clump prior to massive star formation is much smaller because of a lower temperature ($< 20 \text{ K}$) in these regions (Pillai et al. 2006). In a sequence of evolution, cores that give rise to massive stars must be relatively cold in the early stage due to a lack of strong stellar heating, and later enter the hot core phase characterized by strong emission from organic molecules as a result of evaporation of grain mantles and subsequent high temperature gas phase chemistry. In contrast to hot molecular cores with embedded high-mass protostars, we refer entities that ultimately form massive stars, *i.e.*, precursors of hot molecular cores, as *cold cores*. What is typical mass of these cold cores? Do they contain $10^2 M_\odot$ as postulated in some theoretical models (McKee & Tan 2002)? Studies of infrared dark clouds (IRDCs), massive clouds at low temperatures and high densities (Egan et al. 1998; Carey et al. 1998, 2000; Hennebelle et al. 2001; Simon et al. 2006b,a; Rathborne et al. 2006), can provide clues to these questions, and shed light on the process of massive star formation.

¹We refer a molecular clump as an entity with a size scale of 1 pc, which is capable of forming a cluster of stars, while a molecular core as an entity with a size scale of 0.1 pc, which forms one or a small group of stars.

²Jeans mass $M_J = \frac{\pi^{5/2} C_s^3}{6\sqrt{G^3 \rho}}$, where C_s is the sound speed, and ρ the mass density

Zhang et al. (2009) reported 1.3mm continuum image of a massive molecular clump P1 in IRDC G028.34+00.06 (hereafter G28.34), obtained with the Submillimeter Array. This clump contains more than $10^3 M_\odot$ of dense gas, with a low luminosity of a few $100 L_\odot$ (Wang et al. 2008). Arcsecond resolution observations resolved the molecular clump into five dense cores with masses of 22 to $64 M_\odot$ separated by 0.14 to 0.2 pc. The gas temperature, measured at $3'' - 4''$ resolution with the NH_3 (J, K) = (1,1) and (2,2) amounts to 13 to 16 K in these cores (Wang et al. 2008). The average gas temperature and density in the clump yield a thermal Jeans mass of $1 M_\odot$, 1 to 2 orders of magnitude smaller than the mass of the cores. On the other hand, the core masses are compatible with the turbulent Jeans mass³, characterized by the FWHM linewidth of 1.7 km s^{-1} .

The study of G28.34 is insightful in revealing the properties of cold cores. Here, we present results from SMA, VLA and GBT of a massive IRDC clump G030.88+00.13 (hereafter G30.88) with a mass and luminosity similar to G28.34. The object, which is dark from 8 to $24 \mu\text{m}$ in the Spitzer images, contains a mass of $> 10^3 M_\odot$ estimated from $850 \mu\text{m}$ continuum emission, embedded in a $20,000 M_\odot$ cloud seen in CO (Swift 2009). The region, at a reported kinematic distance of 6.7 to 7.2 kpc, has a luminosity of only $460 L_\odot$ (Swift 2009). Swift (2009) presented arcsecond resolution image at $870 \mu\text{m}$ with the SMA, which identified a massive core of $110 M_\odot$. The NH_3 data from the new VLA and GBT observations in this paper reveal two velocity components along the line of sight: One component coincides with the IRDC G30.88. The other component, likely at a different distance, is associated with the massive core detected with the SMA and an H_2O maser emission. No compact cores more massive than $8 M_\odot$ (4σ) are found to be associated with the IRDC clump. Thus, this IRDC component may represent a precluster clump. In Section 2 we presents details of the observations. Section 3 presents the main results and the implications of the findings to cold core formation and evolution.

³Turbulent Jeans mass follows the same formula as the thermal Jeans mass ($M_J = \frac{\pi^{5/2} C_s^3}{6\sqrt{G^3 \rho}}$), but with the sound speed C_s replaced by the turbulent velocity. Turbulence can be highly anisotropic at large spatial scales. In the analysis, we assume isotropic turbulence at the scale of dense cores.

2. Observations

2.1. VLA

We observed IRDC G30.88 in the NH_3 (J, K) = (1,1) and the (2,2) lines with the VLA⁴ on 2010 January 8 in its D configuration. The phase center of the observations was RA(J2000) = 18:47:13.70, Dec (J2000) = −01:45:03.70. The 25m-dish of the VLA antennas yields a FWHM primary beam of approximately $2'$ at the observing frequencies. We employed the 2IF mode that splits the 256-channel correlator into two sections to observe the NH_3 (1,1) and (2,2) lines simultaneously in one polarization for each line. The channel separation was 24.4 KHz ($\sim 0.3 \text{ km s}^{-1}$ at the line frequencies). The time variation of antenna gains was calibrated using QSO J1851+005, observed at a cycle of about 20 mins. The absolute flux density is established by bootstrapping to 3C286. The bandpass is calibrated via observations of 3C454.3.

Subsequently, we observed the NH_3 (J, K) = (3,3) line with the EVLA on 2010 May 09 in its D configuration. We observed two polarizations using a bandwidth of 4 MHz that splits into 256 channels. The time variation of antenna gains was calibrated using QSO J1851+005, observed at a cycle of about 6 mins. The absolute flux density is established by bootstrapping to 3C48. The bandpass is calibrated via observations of 3C454.3.

Data on the 22 GHz H_2O maser transition were obtained with the EVLA on 2010 December 16 in its C configuration. We observed two polarizations using a bandwidth of 4 MHz that splits into 64 channels. The time variation of antenna gains was calibrated using QSO J1851+005, observed at a cycle of about 7 mins. The absolute flux density is established by bootstrapping to 3C48. The bandpass is calibrated via observations of 3C454.3.

The visibilities were calibrated and imaged using the AIPS/CASA software packages of the NRAO. The synthesis beam is about $4'' \times 3''$ for the D array data, and $2'' \times 1''$ for the C array data. The detailed observational parameters are summarized in Table 1.

2.2. GBT

Observations of G30.88 were carried out with the Green Bank Telescope (GBT)¹ in the NH_3 (J,K) = (1,1), (2,2), (3,3), and (4,4) transitions during 2010 February 27 through March 1, and 2010 April 29. We used the K-band receiver and a spectrometer setup in the

⁴The National Radio Astronomy Observatory is operated by Associated Universities, Inc., under cooperative agreement with the National Science Foundation.

frequency switching mode that covers four windows, each with 12.5 MHz bandwidth split into 4096 channels. System temperatures varied from 50 to 100 K during the observations mostly due to changes in elevation. The 100m aperture of the GBT gives a $30''$ FWHM in the primary beam. Data were processed using GBTidl. We only present data of the (3,3) line in this paper.

2.3. SMA

Observations with the SMA⁵ (Ho et al. 2004) were made with 8 antennas in the compact configuration from 2007 July 7 through 2008 June 15, in a mosaic of 18 pointings by Swift (2009). The zenith opacity at 225 GHz were 0.08 to 0.15 for the four nights, with double sideband system temperatures of 400 during the transit. The receivers were tuned to an LO frequency of 351 GHz for the 2007 observations, and 340 GHz for the 2008 observations. Table 1 summarizes the main observational parameters.

The visibility data were calibrated with the IDL superset MIR package developed for the Owens Valley Interferometer. The absolute flux level is accurate to about 25%. After calibrations in MIR, the visibility data were exported to the MIRIAD format for further processing and imaging. The continuum is constructed from line free channels in the visibility domain. We combined the continuum data from four tracks, which yields a 1σ rms of 5.7 mJy and a synthesized beam of about $1.9''$ with the naturally weighting of the visibilities.

3. Results and Discussions

3.1. Dense Molecular Gas and Dust Continuum

Figure 1 shows an overview of the G30.88 region in $24\ \mu\text{m}$ obtained from the Spitzer MIPS GAL (Carey et al. 2009), overlaid with contours of the NH_3 (1,1) emission from the VLA. The $850\ \mu\text{m}$ continuum from the JCMT archive (see also Swift 2009) is also outlined in the yellow contour. The H_2O masers detected with the VLA are marked with the plus sign, and the continuum sources detected with the SMA are marked by the star symbol. At $24\ \mu\text{m}$, G30.88 is dark against the galactic IR background. The IR extinction matched the NH_3 and the $850\ \mu\text{m}$ continuum emission well.

⁵The Submillimeter Array is a joint project between the Smithsonian Astrophysical Observatory and the Academia Sinica Institute of Astronomy and Astrophysics, and is funded by the Smithsonian Institution and the Academia Sinica.

Figure 2 presents the integrated NH_3 (J,K)= (1,1), (2,2) and (3,3) emission from the VLA, the 850 μm continuum from JCMT, and 870 μm continuum from the SMA. The range of velocities for the integrated emission is from 95 through 110 km s^{-1} . The NH_3 data reveal a dense gas filament that follows the dust emission from JCMT (approximately $14''$ resolution). It appears that the NH_3 emission is spatially extended in the (1,1) transition, and becomes far more compact in the (3,3) line. Since the NH_3 emission of the (1,1), (2,2) and (3,3) arises from energy levels of 23K, 65K and 125 K, respectively, a progressively smaller spatial extent in higher excitation lines indicates that the extended NH_3 gas is at relatively lower temperatures.

The SMA observations resolved the dust emission seen at lower resolution into a dominant compact feature as reported in Swift (2009). This source is slightly resolved at a resolution of $1''.9 \times 1''.8$, and consists of two peaks. The maximum and the integrated flux of the source is 119 mJy and 255 mJy, respectively. In addition to the dominant core which we name SMM1, there appear to be emission peaks at a level of 4 to 8 σ rms. We identify all dust peaks above 5 σ rms. Following SMM1, we name other five peaks SMM2 through SMM6, ordered in decreasing fluxes. The parameters of the continuum sources are given in Table 2. Of the six sources, only SMM1 was reported in Swift (2009). With a more accurate temperature measurement (45K, see Section 3.2) for SMM1, we find a gas mass of 32 M_\odot , about 1/3 of the value in Swift (2009). The difference is mainly due to the temperature values used. By comparing the dust peaks with the NH_3 and H_2O data, we confirm that all the dust peaks are robust detections (see Section 3.4).

Figure 3 presents the VLA spectra of the NH_3 (1,1), (2,2) and (3,3) transitions toward SMM1. For comparison, we also present the NH_3 (3,3) spectrum from the GBT for the same position. The NH_3 metastable lines have 18 distinctive hyperfines that normally appear in 5 separate components due to blending (Ho & Townes 1983). For the (1,1) transition, the inner and outer satellite pairs appear at 7.7 and 19.4 km s^{-1} from the main hyperfine. For the (2,2) transition, the inner satellite pair is 16.6 km s^{-1} from the main hyperfine. Both the (1,1) and (2,2) spectra show complex features indicative of multiple velocity components. The (3,3) line, for which the inner hyperfines are further out from the main line and are much fainter, clearly reveals two line-of-sight velocity components, C1 at a V_{LSR} velocity of 97 km s^{-1} , and C2 at 107 km s^{-1} . The relative strength in brightness temperatures between the VLA and GBT spectra indicates that the C2 component is spatially compact, thus is much brighter at a higher angular resolution (0.35 K in GBT versus 5.0 K in the VLA map). On the other hand, the C1 component is more extended: It is detected by the GBT at a peak temperature of 0.2 K, and is not seen in the VLA spectrum at a 1σ rms of 0.5 K. A comparison between the GBT flux and the 1σ rms of the VLA data suggests that the faint (3,3) emission seen in C1 is spatially extended and fills the GBT beam.

3.2. Properties of Two Cloud Components

Due to the crowded hyperfine structures in the $(J,K) = (1,1)$ line, the main hyperfine of the C1 component is blended with the first satellite hyperfine of the C2 component. Since the hyperfines of the $(2,2)$ line are further separated, we compute its moment 0, 1, and 2 maps for the two velocity components, which are presented in Figure 4. As one can see, the morphology of the C1 component is more extended, and correlates well with the extinction feature in the $24\mu\text{m}$ image and sub-millimeter continuum emission from the JCMT. The C2 component is spatially compact and is more centrally peaked than the C1 component. An NH_3 extension to the northeast of SMM1 seen in the C2 component coincides with the IR extinction and probably contributes to the IRDC. However, the integrated flux of the extension amounts only 20% of the integrated flux over the same area in the C1 component. Therefore, IRDC is predominantly associated with the C1 component. SMM1, on the other hand, coincides with the peak of the NH_3 emission of the C2 component, and falls in the trough in the NH_3 emission of the C1 component. Thus, SMM1 is likely associated with the 107 km s^{-1} C2 component. We will further discuss the association of other continuum sources with the two cloud components in Section 3.4.

The LSR velocities of the dense NH_3 gas yield a kinematic distance of 6.5 and 7.3 kpc for the two cloud components, respectively. The integrated fluxes of the NH_3 $(2,2)$ emission within the IR extinction are 1.9 and 1.0 Jy km s^{-1} for the 97 and 107 km s^{-1} components, respectively. The JCMT $850 \mu\text{m}$ flux integrated within the IRDC region amounts to 9 Jy . Assuming that the dust continuum emission from the two components is proportional to the fluxes of the corresponding NH_3 emission, we obtain an $850 \mu\text{m}$ flux of 5.9 Jy for C1, and 3.1 Jy for C2, respectively. Using an average dust temperature of 19 K (see temperature estimate later in this section), a dust opacity law of Hildebrand (1983) with a spectral index of 1.5 , and a dust to gas ratio of $1:100$, we obtain a mass of $1.8 \times 10^3 M_\odot$ for C1, and $1.2 \times 10^3 M_\odot$ for C2. With a size of $40'' \times 26''$ for C1, the average density amounts to $2.0 \times 10^4 \text{ cm}^{-3}$ and $1.0 \times 10^{23} \text{ cm}^{-2}$, respectively. The dust opacity law adopted here gives an opacity value $\kappa(850\mu\text{m}) = 0.015 \text{ cm}^{-2} \text{ g}^{-1}$, consistent with that used in Swift (2009). Adopting a spectral index of 2 for the dust opacity law results in a nearly factor of 2 larger in gas mass.

We estimate the NH_3 gas temperature (Ho & Townes 1983) using the VLA data. Since the hyperfines of the C1 component is blended, we cannot reliably obtain its optical depth. Assuming optically thin emission for the C1 component, we derive a rotational temperature of 20 K . The rotational temperature $T_R(2,2 : 1,1)$ is related to the flux ratio of the main hyperfine component $F(1,1)$ and $F(2,2)$ (see eqn 4 in Ho & Townes 1983) via

$$T_R(2,2 : 1,1) = -41.5 \div \ln\left\{\frac{-0.283}{\tau_m(1,1)} \ln\left[1 - \frac{F(2,2)}{F(1,1)} \times (1 - e^{-\tau_m(1,1)})\right]\right\}.$$

When $F(2, 2) < F(1, 1)$, which is the case for C1, the optically thin assumption causes the rotation temperature to be over estimated. For $\tau_m(1, 1) = 1$ and 5, the gas temperature of 20K under the optically thin assumption becomes 19 and 12 K, respectively. The NH_3 (1,1) emission likely has a moderate optical depth, thus the gas temperature of the C1 component should be lower than 20 K. For the C2 component at 107 km s^{-1} , the NH_3 emission is detected in the (3,3) line toward SMM1. We find a rotation temperature of 45K toward SMM1, and 19 K outside of SMM1.

As shown in Figure 4, the line width of the C1 component revealed by the moment two map is rather uniform, with an average line width of 0.55 km s^{-1} (or a FWHM of 1.4 km s^{-1} ⁶). There appears to be two areas with slightly larger line widths of $> 1 \text{ km s}^{-1}$. The one northeast of SMM1 is due to broadening by a feature at a slightly different velocity as shown in the moment 1 image. The other one $11''$ south of SMM1 has a line width of 2 km s^{-1} . This region coincides with a tentative detection of an SMA peak at $\text{RA(J2000)} = 18:47:13.46$, $\text{Dec(J2000)} = -01:45:13.0$ and with a peak flux of 27 mJy. Since the flux is lower than the 5σ cutoff limit, we do not report the source in Table 2. Future deeper observations will help confirming this dust peak.

The Doppler line width of the C2 component varies from 0.34 (or FWHM of 0.8 km s^{-1}) to 1.3 km s^{-1} (or FWHM of 2.5 km s^{-1}) toward the SMM1 dust peak. Both C1 and C2 components show a velocity gradient. There is a velocity shift of approximately 3 km s^{-1} over a projected length of $40''$ (or 1.7 pc) along the filament in the northeast-southwest direction in C1. For C2, there appears to be a shift of 1 km s^{-1} across SMM1 at a position angle of 60° . This motion is likely due to rotation in the core similar to that found in high-mass protostellar objects (e.g. IRAS 20126+4104 Zhang et al. 1998; Keto & Zhang 2010, G10.6 Keto et al. 1987).

3.3. H_2O Masers

As signposts of star formation, H_2O masers trace protostellar activities of a wide range of stellar masses (Wouterloot & Walmsley 1986; Churchwell et al. 1990; Palla & Stahler 1993; Claussen et al. 1996). Since their excitation requires high density and temperature (Elitzur et al. 1989; Felli et al. 1992), H_2O masers normally arise in the close proximity of a protostar, thus mark the position of the protostar that may not be revealed otherwise. A total of seven H_2O masers are detected in the region. Table 3 reports the maser positions and the peak bright-

⁶If the line profile is Gaussian, the FWHM linewidth is related to the Doppler linewidth by a multiplicative factor of $2\sqrt{2\ln 2}$.

ness temperatures in a descending order. Figure 5 presents the maser spectra. The H_2O maser fluxes reported are not corrected for the primary beam of the VLA. This is because outside the FWHM of the primary beam ($\sim 120''$), a symmetric two dimensional Gaussian profile does not represent the beam accurately. Applying a Gaussian correction to the data may introduce additional error in the maser brightness temperature, especially for masers outside of the FWHM of the primary beam. Should such a correction be applied to the data, the maser feature 2, the one furthest away from the pointing center, is about a factor of 5 brighter.

As seen in Figure 5, all masers exhibit complex spectra and have a broad linewidth of 3 to 8 km s^{-1} . Since a typical maser feature has a line width of $\sim 1 \text{ km s}^{-1}$ as required by coherent amplification, the broad linewidths seen here indicate spatially unresolved maser features in the synthesized beam of $2'' \times 1''$. Masers 1, 2, 6 and 7 have centroid velocities close to 107 km s^{-1} . Therefore, they are likely associated with the C2 cloud component (see more discussions in Section 3.4). On the other hand, maser 4 has a centroid velocity close to 97 km s^{-1} . Thus, it is likely associated with the 97 km s^{-1} component. We caution that masers are often excited in protostellar outflows, and may have velocities offset from that of the cloud. This is shown in masers 3, and 5, who have features detected close to 97 and 107 km s^{-1} . We will discuss associations of the dust continuum sources and H_2O masers with the thermal NH_3 gas in Section 3.4.

Other than SMM1 and SMM5, no other SMA dust peaks coincide with H_2O masers. On the other hand, most H_2O masers are associated with either NH_3 peaks, mid-IR sources or with the JCMT 850 μm continuum emission.

3.4. Association of SMA Dust Peaks and H_2O Masers with the NH_3 Gas

The continuum image from the SMA reveals at least six dust peaks with masses of 18 to 40 M_\odot . Except spatially extended CO, no other molecular line emissions are detected toward most of the dust peaks despite a total passband of 4 GHz. Thus, we cannot determine the V_{LSR} velocity of these continuum sources based on the SMA data. In this section, we compare the spatial positions of the SMA dust peaks with the NH_3 (1,1) data and the H_2O positions from the VLA to determine the association of the sources with the two cloud components. Figure 6 presents the NH_3 (1,1) channel maps of the two cloud components with dust continuum peaks and H_2O maser positions. It is clear that SMM1, the dominant dust peak, coincides with the peak NH_3 emission (see velocity channels with V_{LSR} of 106.3 through 106.9 km s^{-1} and 109.1 through 109.7 km s^{-1} in Figure 6b). In addition, the peak velocity of the maser feature 1 is also close to the cloud velocity of component C2. Therefore, SMM1

and maser 1 are associated with the C2 component. The dust cores SMM2, SMM3, SMM4 and maser 3 are aligned in the north-south direction, and coincide with an NH_3 filament (see channels with V_{LSR} of 106.9 through 109.4 km s^{-1} in Figure 6b). Thus, they are likely associated with the C2 cloud component. SMM5 and maser 4 are not close in projection to any NH_3 emission in the C2 component, but is in close proximity of the extended NH_3 emission in the velocity channel of 95.8 km s^{-1} . Since SMM5/maser 4 lie outside of the primary beam of the VLA, the extended NH_3 emission is attenuated. Given that the maser velocity is close to that of the C1 cloud, we suggest that SMM5/maser 4 are associated with the C1 component. Finally, SMM6 coincides with the NH_3 emission in V_{LSR} of 106.3 through 107.2 km s^{-1} and 97.3 through 98.2 km s^{-1} . It appears that the NH_3 (1,1) emissions in 106.3 through 107.2 km s^{-1} are more centrally peaks. Therefore, we tentatively assign SMM6 to the C2 cloud component. No strong NH_3 emissions are detected toward masers 6 and 7. The peak velocities of the masers, however, indicate that they are associated with the C2 component. Tables 2 and 3 summarize the association of the SMA dust peaks and H_2O masers with the two cloud components.

3.5. Nature of the C2 Clump: A Massive Protocluster in the Making

It appears that the majority of the SMA dust peaks (SMM1, SMM2, SMM3, SMM4, SMM6), and H_2O masers (1,2,3,6,7) are associated with the C2 cloud component. The presence of H_2O maser emission indicates protostellar activities. The dominant dust continuum source, SMM1, is the only continuum source associated with strong NH_3 (3,3) emission from the warm gas of 45 K. Other continuum sources are not detected in NH_3 (3,3) and are associated with gas of about 19 K.

Assuming that the dust is in a thermodynamic equilibrium with the gas in this high density environment, we approximate the dust temperature by the NH_3 gas temperature. For a dust temperature of 45 K and a source size of 1.1'' for SMM1, we estimate a luminosity of 420 L_{\odot} for SMM1 following Scoville & Kwan (1976). This value is consistent with the luminosity of 460 L_{\odot} in Swift (2009), derived from the spectral energy distribution. These luminosities correspond to a zero age main sequence star of 5 M_{\odot} . Since the star is under active accretion, which contributes to the total luminosity, the stellar mass is likely smaller. This young protostar is surrounded by 32 M_{\odot} of dense gas within a scale of 0.04 pc, and several $10^3 M_{\odot}$ gas on larger scales. There is a large reservoir of dense gas for the protostar to accrete. The amount of dense gas and the size scale of the molecular clump are similar to those that harbor massive stars with bright hypercompact and ultra compact HII regions. For instance, one of the nearest examples of massive star formation, Orion KL, contains a dense

molecular clump of several $10^3 M_{\odot}$ within a scale of 1.5 pc (Chini et al. 1997; Lis et al. 1998; Johnstone & Bally 1999). This region, with a luminosity of $10^5 L_{\odot}$ is forming a cluster of stars (Beuther et al. 2005; Zapata et al. 2009). As a similar example but at a larger distance of 6 kpc, G10.6 is a bright hyper compact HII region embedded in a flattened molecular clump of $> 10^3 M_{\odot}$ in its inner 0.5pc region (Keto et al. 1987; Sollins et al. 2005; Liu et al. 2010). The region has a luminosity of $9 \times 10^5 L_{\odot}$, and contains a cluster of stars of $195 M_{\odot}$ (Sollins et al. 2005) based on its ionization flux and total luminosity. The presence of several massive cores and H_2O masers in G30.88 C2 indicates active ongoing star formation. The similar large amount of dense gas and the low luminosity suggest that the G30.88 C2 region is a younger cousin of Orion KL and G10.6, with the most massive protostar(s) still at an intermediate mass stage. It is reasonable to expect that it will form a massive cluster when accretion is complete.

3.6. Nature of the C1 Clump: A Massive Precluster Clump ?

Beside the tentative detection of the dust peak at $RA(J2000) = 18:47:13.46$, $Dec(J2000) = -01:45:13.0$, there appear to be no dust continuum sources nor H_2O masers associated with the C1 cloud component within the IR dark region. Since the C1 cloud component contains $1.8 \times 10^3 M_{\odot}$ over a scale of 2 pc, similar to that of C2, a lack of compact cores is intriguing. The relatively flat distribution of the NH_3 gas shown in Figure 4 and Figure 6a suggests that C1 is likely at an earlier evolutionary stage than C2, which makes it a candidate for probing the onset of massive star formation.

It is often debated whether massive stars form from the monolithic collapse of cold, dense molecular cores of $10^2 M_{\odot}$ (e.g. Krumholz et al. 2005), or they form as an integral part of a cluster formation in a $10^3 M_{\odot}$ clump (e.g. Bonnell et al. 2004; Li & Nakamura 2004). A key difference between the two pictures is whether cold cores forming massive stars acquire all the mass initially before the birth of a protostar. It appears that the C1 clump bears the closest resemblance in conditions to the onset of a massive star formation. In this clump, we find an upper limit of temperature of 20K, an average density of $2.0 \times 10^4 cm^{-3}$, and a line width of $0.55 km s^{-1}$ (or FWHM of $1.4 km s^{-1}$). There appear to be no massive cold cores of $10^2 M_{\odot}$ detected in the C1 clump, in contrast to what has been assumed in the monolithic collapse model.

However, interferometers filter out spatially extended emission. To test possible bias in the SMA observations, we examine the filtering effect and the ability in detecting faint cores by simulating observations using the JCMT image presented in Figure 2. We choose a single SMA pointing centered at $RA(J2000) = 18:47:12.70$, $Dec(J2000) = -1:45:22.90$ for

the simulation. A single pointing is preferred over simulating multi-field mosaic in order to avoid amplifications of noise toward the edge of the primary beam in mosaic. This particular pointing, which lies in between SMM1 and SMM5, is chosen since it is more than one primary beam away from any dust peaks. Thus, the image is less affected by the side lobes from SMM1. Figure 7 presents a comparison of the SMA data with simulated images. The dust emission model, shown in Figure 7b, is derived from the JCMT image tapered by the SMA primary beam, approximately $34''$ at 345 GHz. The peak flux of the JCMT data is 1.37 Jy at a beam of $14''$. Assuming that the emission is smooth within the $14''$ beam, we derive a flux of 24 mJy per $1''.9 \times 1''.8$ beam. This is about the 4σ noise level of the SMA observations. Therefore, the continuum emission would have been barely detectable with the SMA, if it is smooth and if there was no spatial filtering effect of the interferometer. A simulated observation using the JCMT data as the source model, and using the UV coverage and noise characteristics of the actual SMA data is shown in Figure 7c. As one can see, nearly no emission is detected due to a missing flux. However, if there were a compact core with a flux of 30 mJy embedded in the extended molecular clump as a result of core formation, SMA observations would have reliably detected such an object, as shown in Figure 7d. The fact that SMA does not detect them limits the presence of compact cores of $8 M_{\odot}$ at a 4σ level.

These simulated observations reinforce identification of the dust cores in the SMA image reported in Table 2. In addition, the simulation indicates that at very early stages of massive star formation, no massive cold cores are spatially distinct from the molecular clump. Our study of G30.88 rules out the presence of 0.1 pc cores of $8 M_{\odot}$ at a 4σ level in the C1 region. This implies that cores giving birth to massive stars may not be initially massive (e.g. $10^2 M_{\odot}$).

3.7. Fragmentation and Massive Star Formation

The core masses detected in the G30.88 C2 clump range from 18 to $40 M_{\odot}$. They are likely the sites to form massive stars. A density of $2.0 \times 10^4 \text{ cm}^{-3}$ and a temperature of 19 K yield a thermal Jeans mass of $5 M_{\odot}$, and a Jeans length of 0.2 pc for the region. Although the SMA observations are not deep enough to detect cores of one Jeans mass, the cores revealed here are 4 times or more massive than the Jeans mass, similar to the case seen in the G28.34-P1 clump (Zhang et al. 2009), and G8.68 (Longmore et al. 2011). Assuming an isotropic turbulence for which its velocity is characterized by the NH_3 line width of 0.55 km s^{-1} , we find a turbulent Jeans mass of $37 M_{\odot}$, a value more compatible with the masses detected in the region. This reinforces the notion that massive cores arise from a turbulent supported fragmentation.

Similar to C2, the C1 region contains a large mass of $1.8 \times 10^3 M_{\odot}$. However, in contrast to strong dust cores revealed by the SMA, no apparent compact cores are detected at a 4σ mass of $8 M_{\odot}$. Assuming that C1 and C2 represent two stages along a common evolutionary sequence, this implies that cold cores forming massive stars are probably less massive than $8 M_{\odot}$ initially. These cores will continue to grow in mass by gathering material from the clump, and become compact cores as seen in C2.

An empirical picture of massive star formation appears to emerge from observations in the past several years. Surveys of cluster forming clumps reveal blue-red asymmetry in optically thick tracers (e.g. HCN and HCO^+ , Wu & Evans 2003; Fuller et al. 2005; Wu et al. 2007), consistent with infall of $1 - 2 \text{ km s}^{-1}$ at the cluster forming scale of approximately 1 pc. These surveys with single dish telescopes at $> 10''$ resolution are in agreement with high resolution work in G10.6, in which global infall is observed in both molecular and ionized gas toward a cluster of stars with a total stellar mass of $195 M_{\odot}$ (Ho & Haschick 1986; Keto et al. 1987; Sollins et al. 2005; Liu et al. 2010). Recently, Galván-Madrid et al. (2009) reported studies of an HII region G20.08-0.14, where inverse P-Cygni profiles are detected toward a cluster of HII regions with a linear size of 0.3 pc. The infall motion appears to continue toward a hot molecular core in which the youngest hyper compact HII region is embedded. The wide spread infall motion, together with the fragmentation studies in this paper and Zhang et al. (2009) suggests a picture of massive star formation in a cluster forming environment: Collapse of $10^3 M_{\odot}$ molecular clumps as a result of losing internal turbulent support leads to the formation of dense molecular cores. Among the cores, those leading to the birth of massive stars are more massive than the thermal Jeans mass. How these clumps fragment to super Jeans masses is not certain, but turbulence in these cores appears to be sufficient to provide the support (Zhang et al. 2009). During the early evolution, cores continue to draw material from the molecular clump while the protostar embedded undergoes accretion. This picture is somewhat similar to the competitive accretion by Bonnell et al. (2004). However, it differs in two important aspects: First dense cores harboring massive stars are more massive than the thermal Jeans mass; and secondly, accretion is likely dominated by gas accretion in response to gravity as suggested in Wang et al. (2010), rather than Bondi-Hoyle accretion. This empirical picture is derived from limited observations. ALMA will deliver orders of magnitude improvement in continuum and spectral line sensitivity as compared to current (sub)mm interferometers. More importantly, large number of antennas will improve the dynamic range, and allow detection of lower mass cores in the vicinity of bright objects. It is hopeful that more sensitive studies of cold and massive molecular clumps in the future will lead to a clearer and more complete picture of cluster formation.

4. Conclusion

In conclusion, we present spectral line and continuum images of a massive IRDC G30.88. The cloud appears to consist of two line-of-sight components C1 and C2 with LSR velocities of 97 and 107 km s⁻¹, respectively. Both molecular clumps are massive enough ($> 10^3 M_{\odot}$) to form massive stars, but only C2 exhibits protostellar activities. Among the seven H₂O masers detected with the VLA, five have velocities or positions associated with C2, and none is within the IRDC in C1. The SMA observations reveal six dust features SMM1 through SMM6 with masses from 18 to 40 M_{\odot} , much more massive than the thermal Jeans mass. Among the six cores, five are associated with the C2 region, and one is associated with the C1 component away from the main extinction region. The H₂O maser emission and dust peaks in the C2 clump indicate active star formation, but the low luminosity constrains the protostar(s) at an intermediate mass stage. A lack of dust peaks and H₂O maser emission in C1 puts the IRDC at an even earlier stage of star formation, and does not support the idea of cold cores of $10^2 M_{\odot}$. Observations of G30.88 and other IRDCs such as G28.34 seem to point to the early evolution of massive star formation, in which cores gain mass from the clump while protostars accrete gas from the core.

We thank Jonathan Swift for permission of using the SMA data, and the anonymous referee for comments that improve the clarity of the paper. Q. Z. acknowledges the support from the Smithsonian Institution Endowment Funds. K. W. acknowledges the support from the SMA predoctoral fellowship and the China Scholarship Council.

Facility: Submillimeter Array

Fig. 1: False color 24 μm image from the Spitzer MIPS for the IRDC G30.88 region. The color bar indicates the logarithmic flux scale in units of MJy sr^{-1} . The thin white contours represent the NH_3 (1,1) emission from the VLA. The thick yellow contour outlines the JCMT 850 μm continuum emission. The dashed circle indicates the FWHM primary beam of the NH_3 observations from the VLA. The star symbols mark the dust peaks detected with the SMA. The cross symbols mark the position of the H_2O masers.

Fig. 2: The integrated intensity of the NH_3 (1,1), (2,2) and (3,3) emission from the VLA, the 850 μm emission from JCMT, and 870 μm emission from the SMA. The NH_3 images are contoured at an interval of $15 \text{ mJy beam}^{-1} \times \text{km s}^{-1}$. The JCMT data are plotted at every 10% of the peak (2 Jy beam^{-1}). The SMA data are contoured in steps of 25 mJy beam^{-1} . The star symbols mark the dust peaks detected with the SMA. The cross symbols mark the position of the H_2O masers. The dashed circle indicates the FWHM primary beam of the VLA NH_3 observations. The thin dashed line outlines the 100% sensitivity of the SMA observations. The spatial resolution of each dataset is marked by the shaded ellipse at the bottom-left corner of each panel.

Fig. 3: Spectra of the NH_3 (J, K) = (1,1), (2,2) and (3,3) from the VLA, and the NH_3 (3,3) transition from the GBT toward the position of the SMM1. The two velocity components are marked as “C1” and “C2”.

Fig. 4: Moment 0, 1 and 2 maps of the NH_3 (2,2) line from the VLA for the two velocity components at 97 km s^{-1} (C1), and 107 km s^{-1} (C2) respectively. The contours for the moment 0 map starts at $4 \text{ mJy beam}^{-1} \times \text{km s}^{-1}$ and in increments of the same value. The star symbols mark the dust peaks detected with the SMA. The cross symbols mark the position of the H_2O masers. The synthesized beam is marked at the lower-left corner of each panel.

Fig. 5: H_2O maser spectra for maser features 1, 2, 3, 4, 5, 6, and 7.

Fig. 6: NH_3 (1,1) emission in different velocity channels for the C1 (97 km s^{-1}) component (Fig. 6a) and C2 (107 km s^{-1}) component (Fig. 6b). The contour levels are in steps of 8 mJy beam^{-1} starting from 8 mJy beam^{-1} . The star symbols mark the dust peaks detected with the SMA. The cross symbols mark the position of the H_2O masers. The synthesized beam is marked at the lower-left corner of the first panel. The corresponding LSR velocity of the channel is indicated at the top-right corner of each panel.

Fig. 7: Comparison between the SMA continuum image and simulated observations using the JCMT data as the model. Fig. 7a presents the SMA continuum image at 850 μm from a single pointing centered at $\text{RA}(\text{J2000}) = 18:47:12.70$, $\text{Dec}(\text{J2000}) = -1:45:22.90$. Fig. 7b presents the source model based on the JCMT data tapered by the $34''$ FWHM

primary beam response of the SMA. The contour levels in Fig. 7b are plotted at every 10% of the peak flux of 1.37 Jy per $14''$ beam. Fig. 7c presents the simulated image of the model dust emission in 7b using the UV coverage of the SMA observations. Fig. 7d presents the simulated image of the model in Fig. 7b plus a point source of 30 mJy at $(5'', 5'')$ offset from the pointing center. The contour levels in Figs. 7a,c,d are plotted ± 17 and ± 23 mJy beam $^{-1}$. The synthesized beam in the simulated images is $1''.9 \times 1''.8$, same as the SMA image in Figure 2.

Fig. 1.—

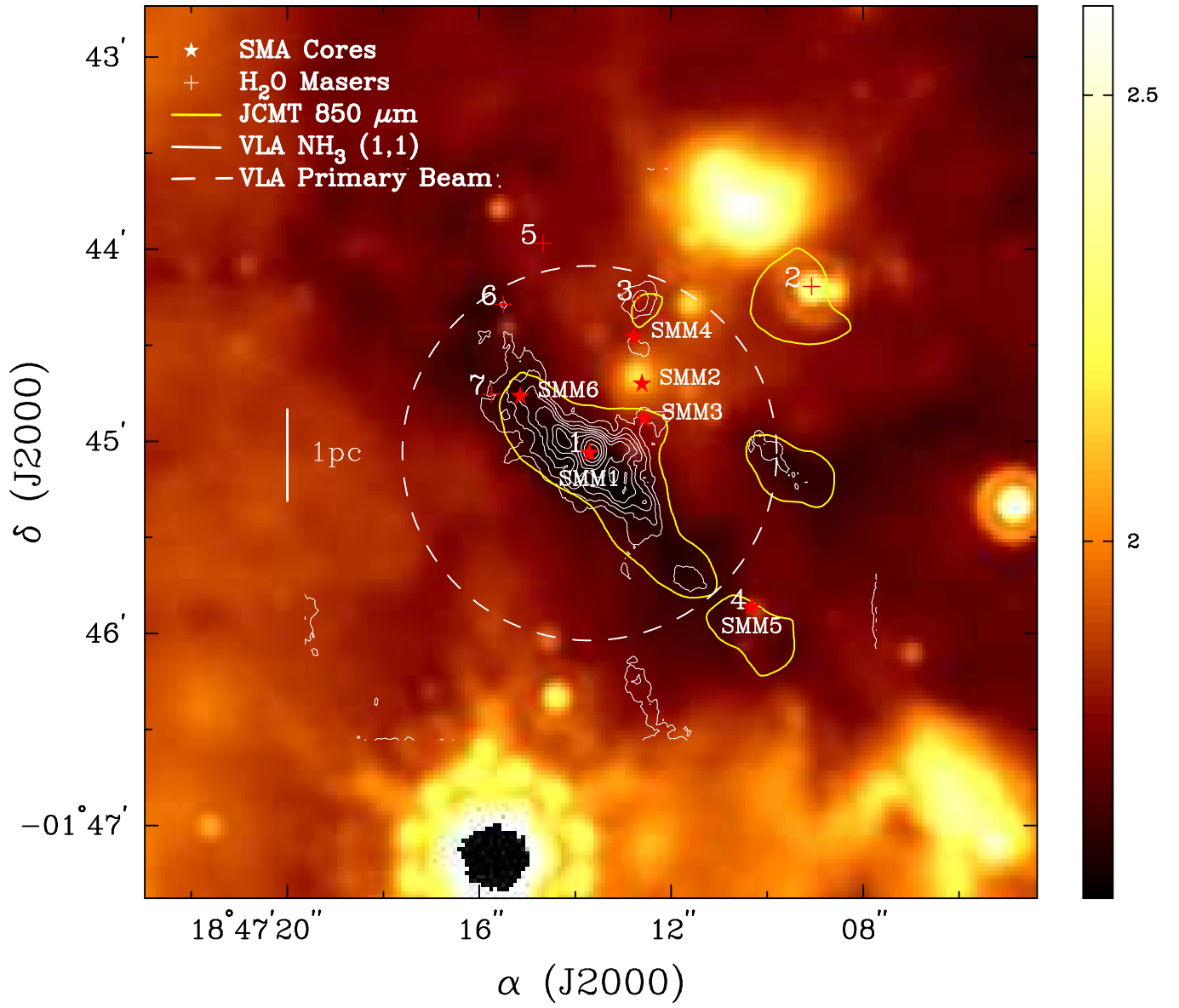


Fig. 2.—

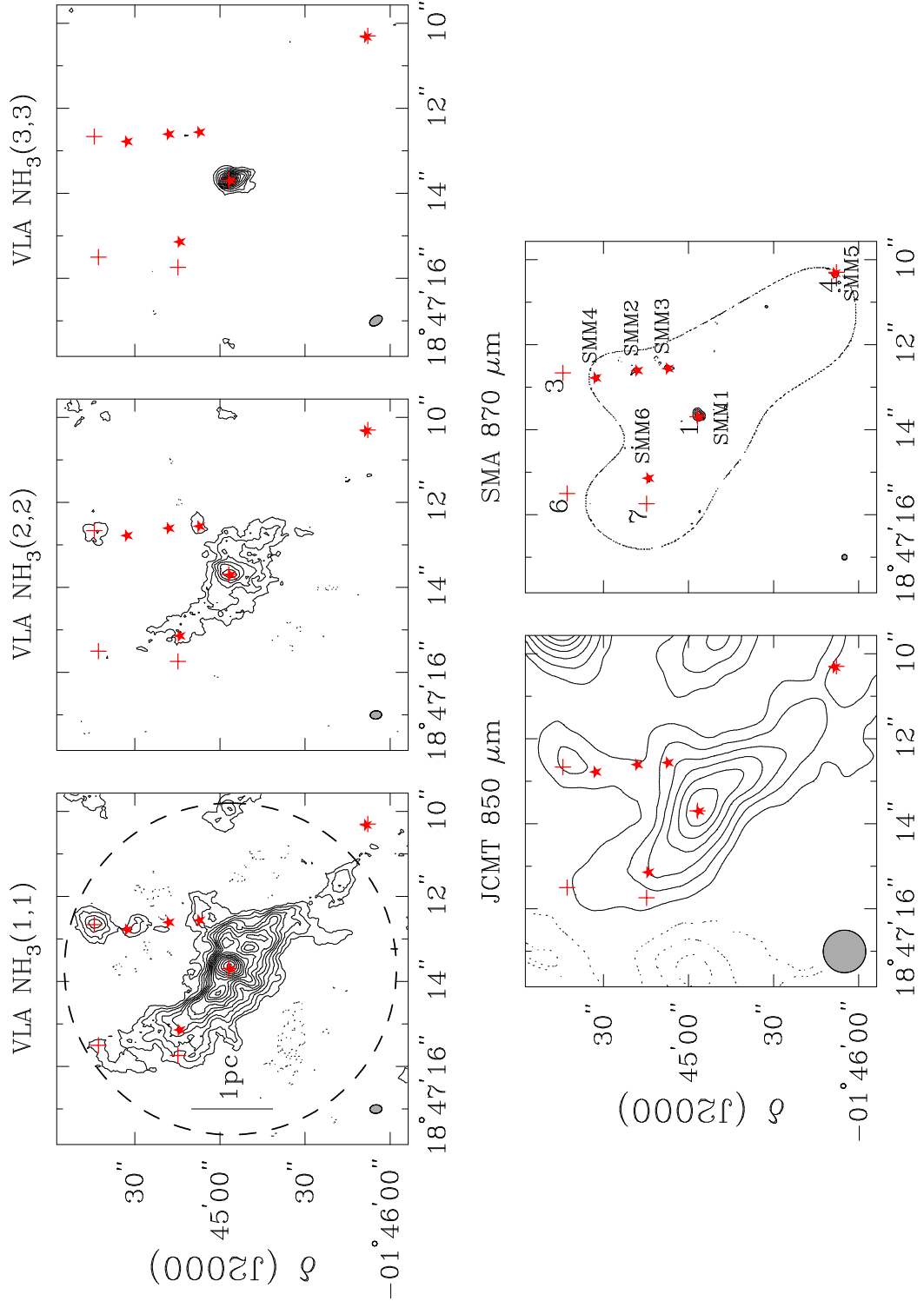


Fig. 3.—

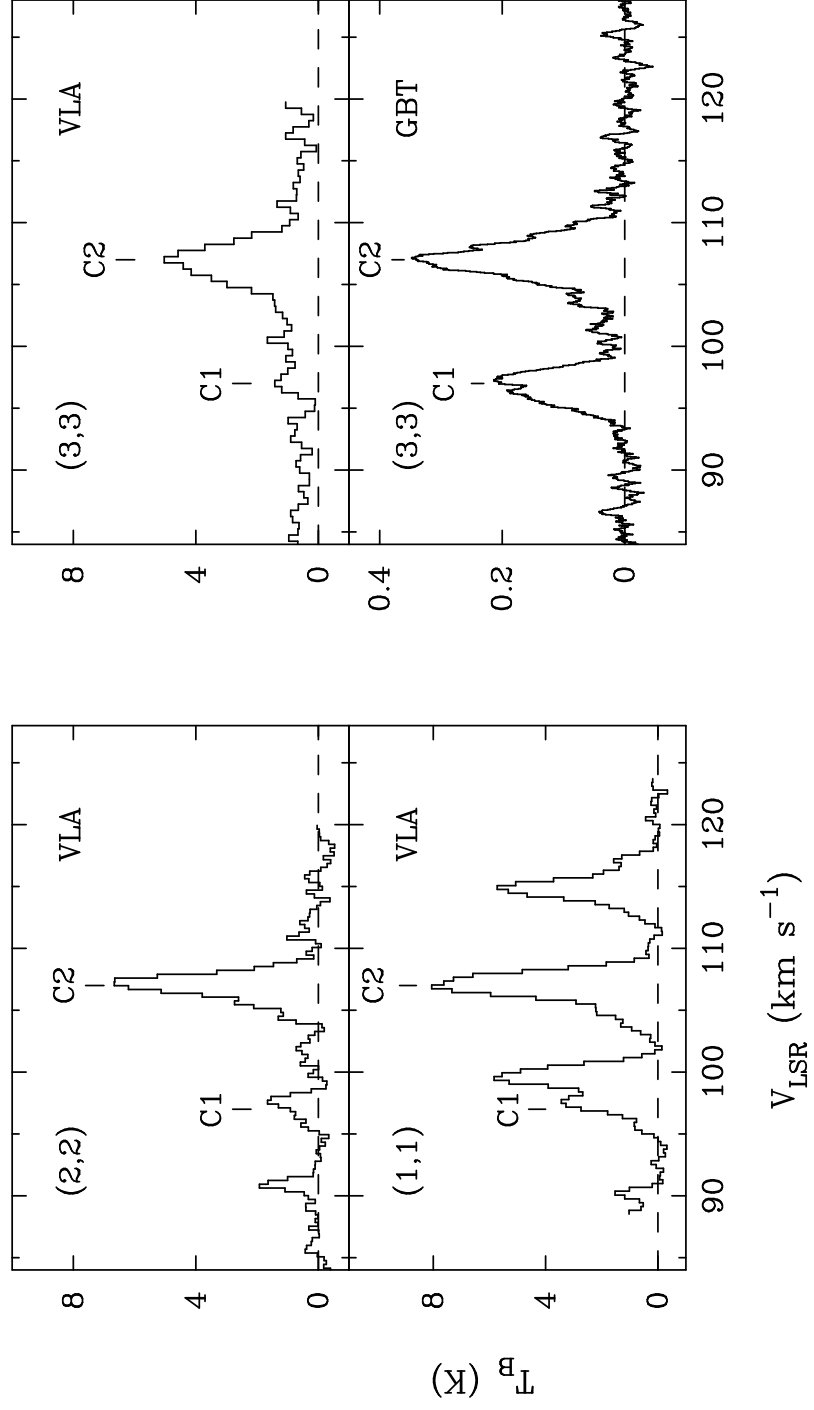


Fig. 4.—

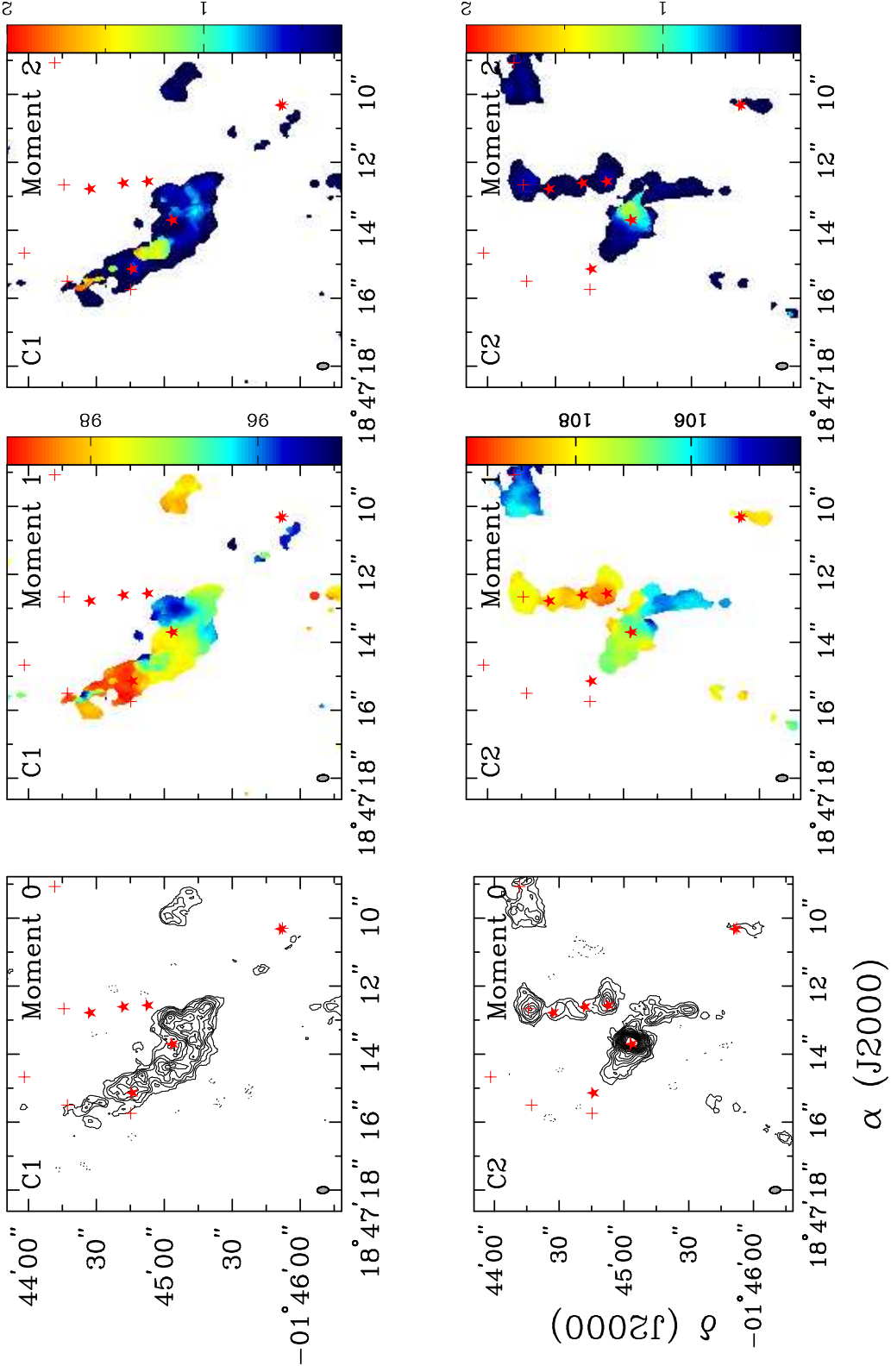


Fig. 5.—

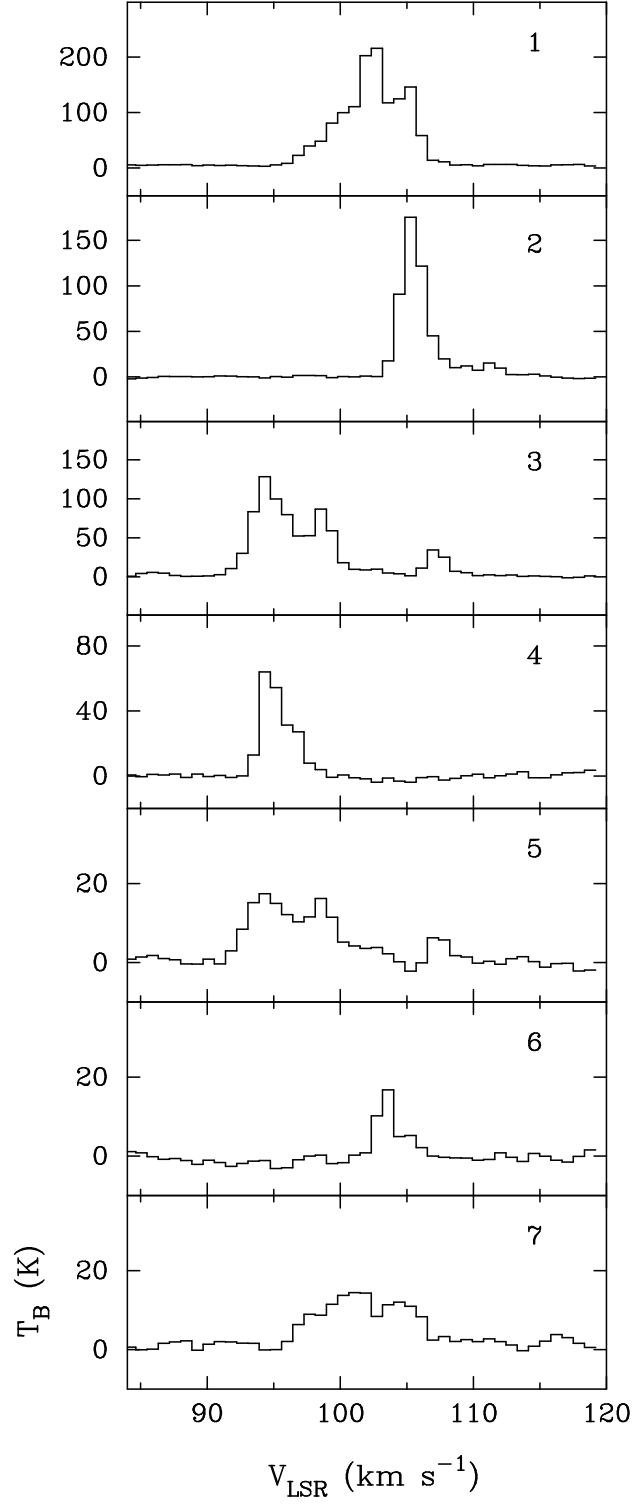


Fig. 6a.—

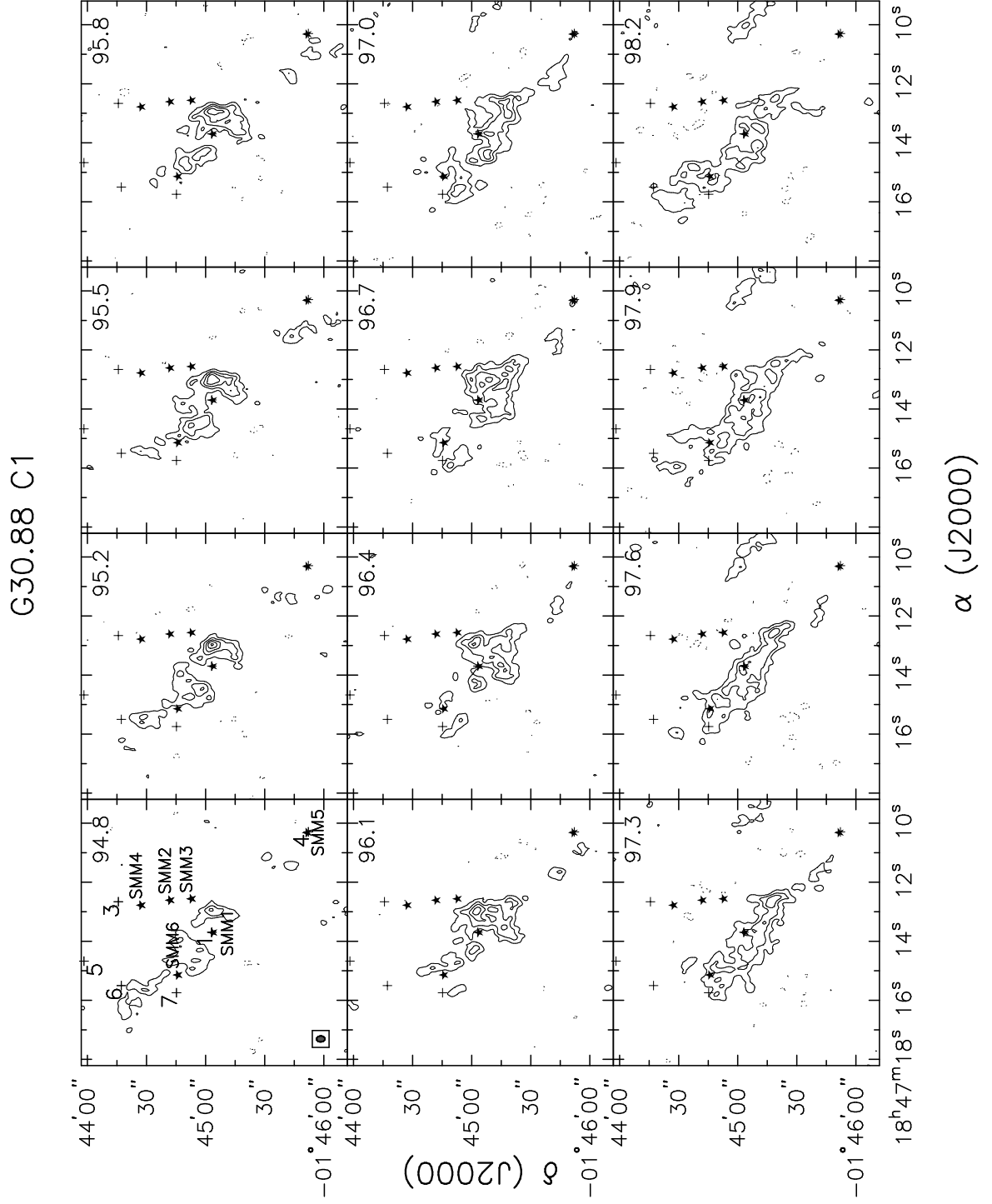


Fig. 6b.—

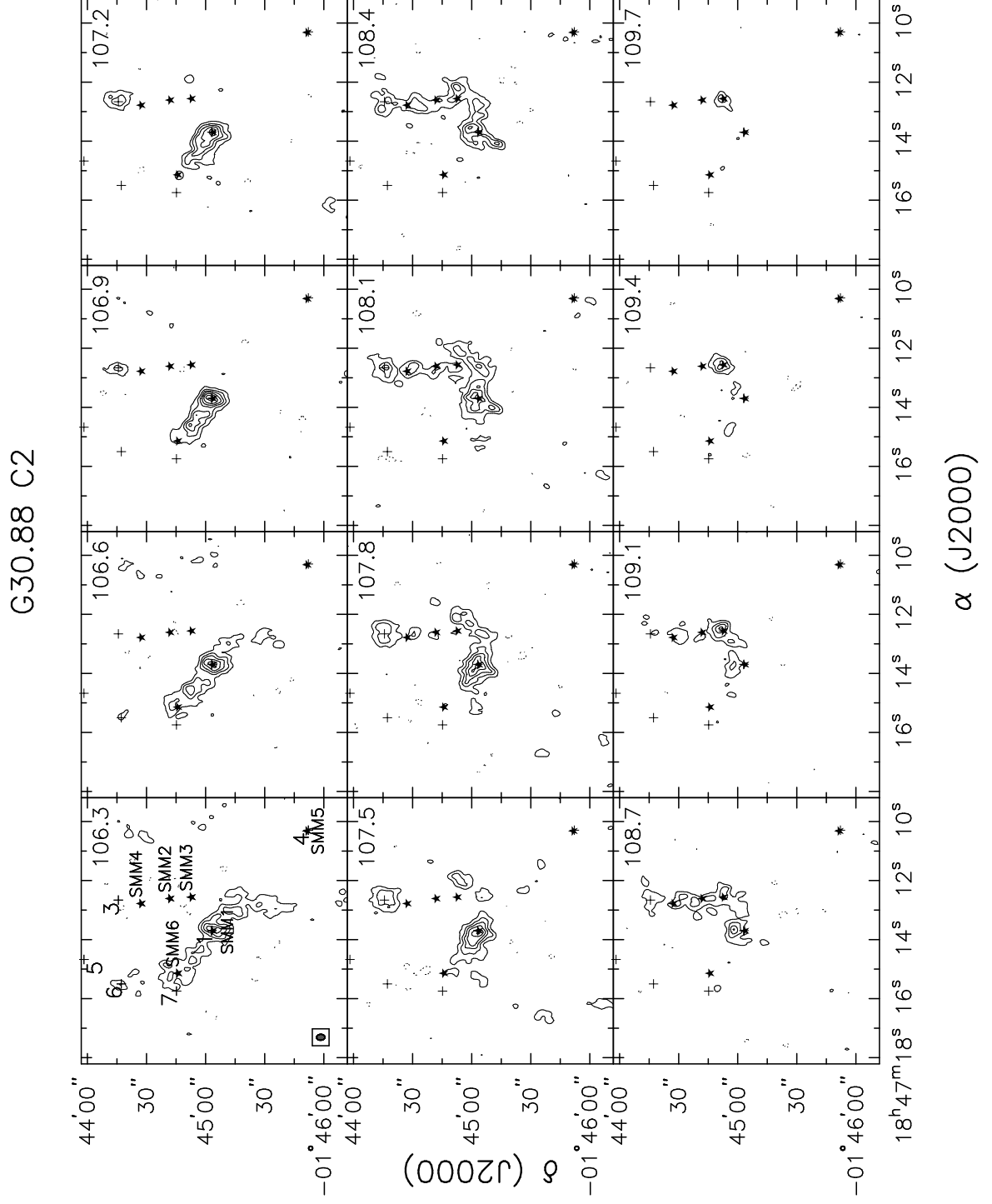
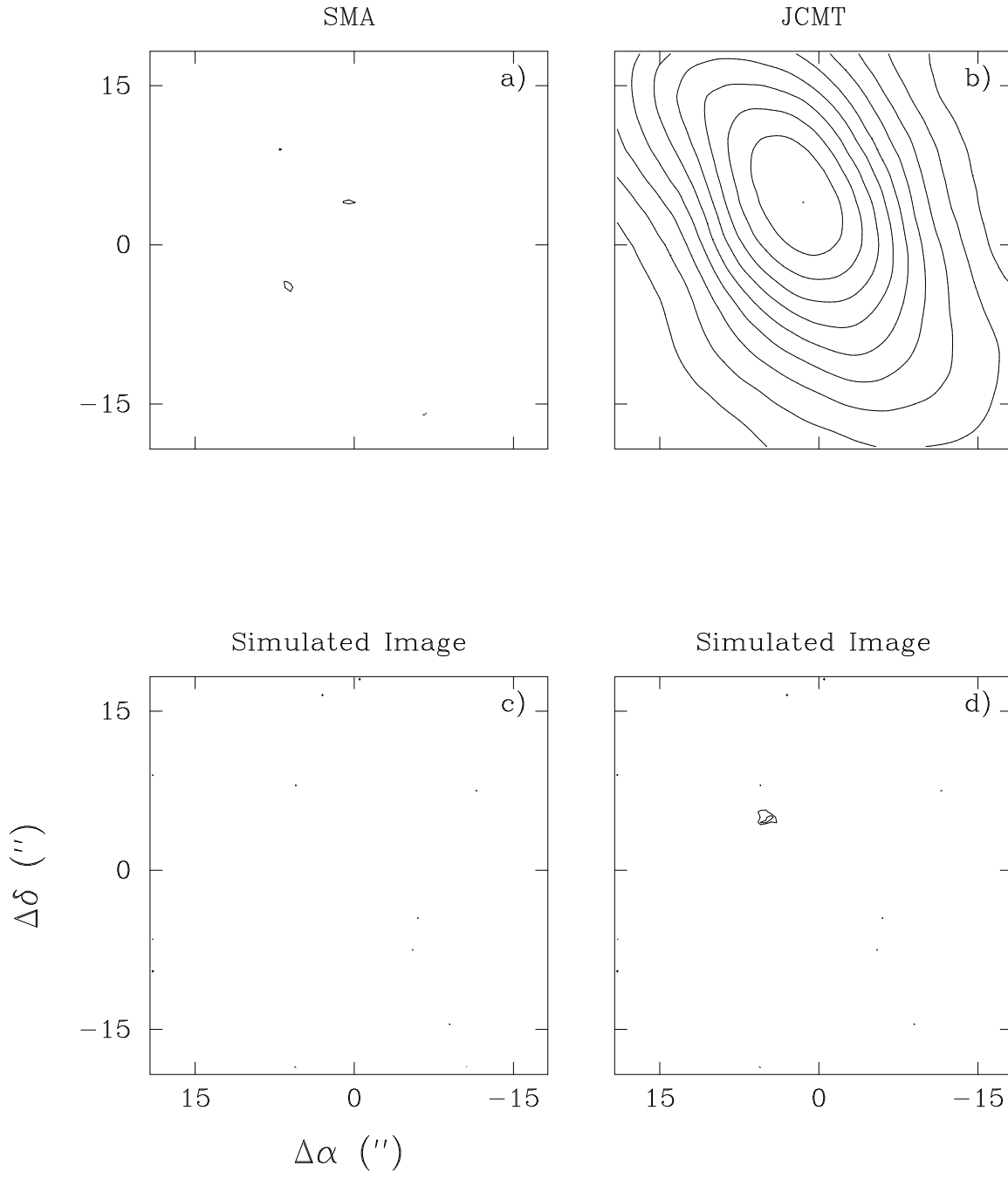


Fig. 7.—



REFERENCES

- Beltrán, M. T., Brand, J., Cesaroni, R., et al. 2006, *A&A*, 447, 221
- Beuther, H., Schilke, P., Menten, K. M., et al. 2002, *ApJ*, 566, 945
- Beuther, H., Zhang, Q., Greenhill, L. J., et al. 2005, *ApJ*, 632, 355
- Bonnell, I. A., Vine, S. G., & Bate, M. R. 2004, *MNRAS*, 349, 735
- Carey, S. J., Clark, F. O., Egan, M. P., et al. 1998, *ApJ*, 508, 721
- Carey, S. J., Feldman, P. A., Redman, R. O., et al. 2000, *ApJ*, 543, L157
- Carey, S. J., Noriega-Crespo, A., Mizuno, D. R., et al. 2009, *PASP*, 121, 76
- Chini, R., Reipurth, B., Ward-Thompson, D., et al. 1997, *ApJ*, 474, L135+
- Churchwell, E., Walmsley, C. M., & Cesaroni, R. 1990, *A&AS*, 83, 119
- Claussen, M. J., Wilking, B. A., Benson, P. J., et al. 1996, *ApJS*, 106, 111
- Egan, M. P., Shipman, R. F., Price, S. D., et al. 1998, *ApJ*, 494, L199
- Elitzur, M., Hollenbach, D. J., & McKee, C. F. 1989, *ApJ*, 346, 983
- Felli, M., Palagi, F., & Tofani, G. 1992, *A&A*, 255, 293
- Fuller, G. A., Williams, S. J., & Sridharan, T. K. 2005, *A&A*, 442, 949
- Galván-Madrid, R., Keto, E., Zhang, Q., et al. 2009, *ApJ*, 706, 1036
- Garay, G. & Lizano, S. 1999, *PASP*, 111, 1049
- Hennebelle, P., Péroult, M., Teyssier, D., & Ganesh, S. 2001, *A&A*, 365, 598
- Hildebrand, R. H. 1983, *QJRAS*, 24, 267
- Ho, P. T. P. & Haschick, A. D. 1986, *ApJ*, 304, 501
- Ho, P. T. P., Moran, J. M., & Lo, K. Y. 2004, *ApJ*, 616, L1
- Ho, P. T. P. & Townes, C. H. 1983, *ARA&A*, 21, 239
- Johnstone, D. & Bally, J. 1999, *ApJ*, 510, L49
- Keto, E. & Zhang, Q. 2010, *MNRAS*, 648

- Keto, E. R., Ho, P. T. P., & Haschick, A. D. 1987, *ApJ*, 318, 712
- Krumholz, M. R., McKee, C. F., & Klein, R. I. 2005, *Nature*, 438, 332
- Lada, C. J. & Lada, E. A. 2003, *ARA&A*, 41, 57
- Larson, R. B. 2005, *MNRAS*, 359, 211
- Li, Z. & Nakamura, F. 2004, *ApJ*, 609, L83
- Lis, D. C., Serabyn, E., Keene, J., et al. 1998, *ApJ*, 509, 299
- Liu, H., Ho, P. T. P., Zhang, Q., et al. 2010, *ApJ*, 722, 262
- Longmore, S. N., Pillai, T., Keto, E., Zhang, Q., & Qiu, K. 2011, *ApJ*, 726, 97
- McKee, C. F. & Tan, J. C. 2002, *Nature*, 416, 59
- Molinari, S., Brand, J., Cesaroni, R., & Palla, F. 2000, *A&A*, 355, 617
- Palla, F. & Stahler, S. W. 1993, *ApJ*, 418, 414
- Pillai, T., Wyrowski, F., Carey, S. J., & Menten, K. M. 2006, *A&A*, 450, 569
- Rathborne, J. M., Jackson, J. M., & Simon, R. 2006, *ApJ*, 641, 389
- Rathborne, J. M., Simon, R., & Jackson, J. M. 2007, *ApJ*, 662, 1082
- Scoville, N. Z. & Kwan, J. 1976, *ApJ*, 206, 718
- Simon, R., Jackson, J. M., Rathborne, J. M., & Chambers, E. T. 2006a, *ApJ*, 639, 227
- Simon, R., Rathborne, J. M., Shah, R. Y., Jackson, J. M., & Chambers, E. T. 2006b, *ApJ*, 653, 1325
- Sollins, P. K., Zhang, Q., Keto, E., & Ho, P. T. P. 2005, *ApJ*, 624, L49
- Swift, J. J. 2009, *ApJ*, 705, 1456
- Wang, P., Li, Z., Abel, T., & Nakamura, F. 2010, *ApJ*, 709, 27
- Wang, Y., Zhang, Q., Pillai, T., Wyrowski, F., & Wu, Y. 2008, *ApJ*, 672, L33
- Wouterloot, J. G. A. & Walmsley, C. M. 1986, *A&A*, 168, 237
- Wu, J. & Evans, II, N. J. 2003, *ApJ*, 592, L79

- Wu, Y., Henkel, C., Xue, R., Guan, X., & Miller, M. 2007, *ApJ*, 669, L37
- Zapata, L. A., Schmid-Burgk, J., Ho, P. T. P., Rodríguez, L. F., & Menten, K. M. 2009, *ApJ*, 704, L45
- Zhang, Q., Hunter, T. R., & Sridharan, T. K. 1998, *ApJ*, 505, L151
- Zhang, Q., Wang, Y., Pillai, T., & Rathborne, J. 2009, *ApJ*, 696, 268

Table 1: List of Observational Parameters

Instrument	Date of Observations	Line	Bandwidth (MHz)	Spectral Res. (km s ⁻¹)	rms (mJy)	Angular Res. (")
VLA-D	2010/01/08	NH ₃ (1,1),(2,2)	3.12	0.64	2.5	4 × 3
VLA-D	2010/05/09	NH ₃ (3,3)	4	0.20	2.5	4 × 3
VLA-C	2010/11/24	H ₂ O	4	0.84	1.5	2 × 1
GBT	2010/02/27	NH ₃ (1,1),(2,2)	8	0.025	20	30
	–	(3,3),(4,4)				
SMA Compact	2007/07/07	–	4000	–	5.7 ^a	1.9 × 1.8
SMA Compact	2007/10/19	–	4000	–		
SMA Compact	2008/06/02	–	4000	–		
SMA Compact	2008/10/15	–	4000	–		

^a1 σ rms in the combined SMA image.

Table 2: Physical Parameters of Cores

Name	R.A.(J2000) (^h ^m ^s)	Dec.(J2000) ([°] ['] ^{''})	Flux ^a (Jy)	Mass ^b (M _☉)	Association ^c
SMM1	18:47:13.68	-01:45:03.6	0.26	32	C2
SMM2	18:47:12.61	-01:44:42.1	0.10	40	C2
SMM3	18:47:12.56	-01:44:52.9	0.082	33	C2
SMM4	18:47:12.78	-01:44:27.4	0.067	27	C2
SMM5	18:47:10.32	-01:45:51.7	0.060	19	C1
SMM6	18:47:15.14	-01:44:46.0	0.044	18	C2

^aIntegrated flux.

^bWe adopt dust temperatures of 45 K for SMM1, and 19 K for SMM2 through SMM6. We use a dust emissivity index β of 1.5, and the dust opacity law of Hildebrand (1983). The source distances used are 6.5 kpc for the C1 clump and 7.3 kpc for the C2 clump, respectively.

^cAssociation of dust continuum sources with the two cloud components.

Table 3: Properties of H₂O Masers

Name	R.A.(J2000) (^h ^m ^s)	Dec.(J2000) ([°] ['] ^{''})	Flux ^a (K)	Association ^b
1	18:47:13.70	-01:45:03.2	215.8	C2
2	18:47:09.07	-01:44:11.7	175.4	C2
3	18:47:12.67	-01:44:15.7	128.3	C2
4	18:47:10.30	-01:45:52.2	64.0	C1
5	18:47:14.67	-01:43:58.2	17.4	C1
6	18:47:15.50	-01:44:17.2	16.8	C2
7	18:47:15.74	-01:44:45.2	14.4	C2

^aTo avoid introducing additional error, brightness temperatures reported here are not corrected for the primary beam attenuation. Assuming a Gaussian primary beam with a FWHM of 120'', we find a peak brightness temperature of 808.6 K for maser feature 2, a maser knot outside the FWHM of the primary beam. The Jansky to Kelvin conversion factor is $1.11 \times 10^3 \text{ Jy K}^{-1}$.

^bAssociation of the H₂O masers with the two cloud components.